D6

LOW SPEED AIRFOIL DESIGN AND ANALYSIS

6

Richard Eppler
Universität Stuttgart, West Germany

Dan M. Somers
NASA Langley Research Center

SUMMARY

A low speed airfoil design and analysis program has been developed which contains several unique features. In the design mode, the velocity distribution is not specified for one but many different angles of attack. Several iteration options are included which allow the trailing edge angle to be specified while other parameters are iterated. For airfoil analysis, a panel method is available which uses third-order panels having parabolic vorticity distributions. The flow condition is satisfied at the end points of the panels. Both sharp and blunt trailing edges can be analyzed. The integral boundary layer method with its laminar separation bubble analog, empirical transition criterion, and precise turbulent boundary layer equations compares very favorably with other methods, both integral and finite-difference. Comparisons with experiment for several airfoils over a very wide Reynolds number range were very favorable. Applications to high lift airfoil design were also demonstrated.

INTRODUCTION

The application of potential flow theory together with boundary layer theory to airfoil design and analysis was accomplished many years ago. Since that time, high speed computers have allowed results to be obtained more cheaply and quickly than through the use of wind tunnels. Accordingly, the tendency today is toward more and more commonly applicable computer programs. The programs reduce the amount of required wind tunnel testing to that of fundamental phenomena and allow airfoils to be tailored to each specific application.

The program described in this paper has been developed over the past 20 years. We hope to demonstrate that it has reached a stage where some progress can be made in low speed airfoil design and analysis.

This paper does not repeat all of the details included in other papers. Special emphasis is given, however, to those features which are new or different from those in other mathematical models.

SYMBOLS

C_f	skin-friction coefficient
c	airfoil chord
c_d	section profile-drag coefficient
c_l	section lift coefficient
c_m	section pitching-moment coefficient about quarter-chord point
H_{12}	shape factor, $\frac{\delta_1}{\delta_2}$
H_{32}	shape factor, $\frac{\delta_3}{\delta_2}$
l	length
P	point
R	Reynolds number based on free-stream conditions and airfoil chord
R_{δ_2}	Reynolds number based on local conditions and boundary layer momentum thickness
t	thickness of airfoil
U	free-stream velocity
u	local velocity on airfoil
V	velocity; main pressure recovery design variable
x	airfoil abscissa; length
α	angle of attack relative to zero-lift line, deg
α^*	angle of attack relative to zero-lift line for velocity specification in design method, deg
δ_1	boundary layer displacement thickness
δ_2	boundary layer momentum thickness
δ_3	boundary layer energy thickness
ν	kinematic viscosity
ω	total amount of pressure recovery

ω' initial slope of pressure recovery

Subscripts:

l lower surface; local point on airfoil

lm lower surface main pressure recovery

N last point on airfoil

n variable number

u upper surface

um upper surface main pressure recovery

∞ free-stream conditions

DISCUSSION

Inviscid Method

The potential flow part of the mathematical model is incompressible at this time. Two different modes of operation are available.

Design mode.- The first mode is the inverse or design method described in references 1 and 2. This method differs from other inverse methods in that the velocity distribution is not specified for only one angle of attack. Instead, angles of attack which will result in constant velocity over specified segments of the airfoil are input. In other words, pairs of parameters are specified: the first being the segment of the airfoil; the second, the angle of attack relative to the zero-lift line, α^*, which will result in constant velocity over that segment. (See fig. 1.) Of course, some matching conditions must be met to guarantee a smooth velocity distribution for all angles of attack. Toward the trailing edge, on both surfaces, a main pressure recovery can be specified. Finally, a short closure contribution must be introduced to insure that the trailing edge will be closed. The example airfoil shown in figure 1 is specified by the following:

(1) For the upper surface segment from the trailing edge forward to about $x/c = 0.15$, $\alpha^* = 8^0$. Within this segment, the main pressure recovery is specified starting at $x/c = 0.50$.

(2) For the upper surface segment from $x/c = 0.15$ to 0.05, $\alpha^* = 10^0$.

(3) For the upper surface segment from $x/c = 0.05$ to the leading edge, $\alpha^* = 12^0$.

(4) For the entire lower surface, $\alpha^* = 2^0$. The main pressure recovery on the lower surface is specified starting at about $x/c = 0.45$.

In reality, the segments corresponding to the various α^* values are not specified in x/c but rather in the conformal mapping plane in which the airfoil is represented by a circle. So far, no difficulties have arisen in correlating the arcs of the circle with the segments of the airfoil.

It should be remembered that for any given velocity distribution there does not necessarily exist a "normal" airfoil. For example, the closure contributions could be quite large which would result in a very large trailing edge angle. The closure contributions could also give rise to a region of negative thickness near the trailing edge. Accordingly, several iteration options have been included which allow the trailing edge angle to be specified while certain α^* values or the total amount of pressure recovery is iterated. The choice of iteration option allows questions such as the following to be answered: What laminar bucket width is possible given a certain amount of pressure recovery? What amount of pressure recovery is required to produce the desired laminar bucket width? The iteration option selected for the example airfoil iterates the amount of upper and lower surface pressure recovery while holding the α^* values fixed.

Analysis mode.- The second mode of operation is an airfoil analysis method. The method employs panels with distributed surface singularities (fig. 2). The panels are defined by a third-order spline fit of the airfoil coordinates with the end points of the panels being the input airfoil coordinates themselves. The surface singularities consist of a parabolic vorticity distribution. The flow condition, which requires the inner tangential velocity to be zero, is satisfied at each airfoil coordinate (i.e., at the end points of the panels, not the mid-points). Thus, no restrictions are placed on the point distribution, no smoothing or rearranging of the coordinates is performed, only the original airfoil coordinates are used. An option is included, however, by which additional points can be splined in between the original coordinates. This option is helpful if a portion of the airfoil has a sparse number of points or if part of the airfoil is to be geometrically rotated about a flap hinge point. In the latter case, the connection between the forward portion of the airfoil and the flap is defined by an arc consisting of additional points which are generated automatically according to an input length.

As in other panel methods, a singularity arises from the circulation around the airfoil which is unconstrained unless required to satisfy a Kutta condition. Two different cases are involved.

The first case is a sharp trailing edge having either a zero or non-zero angle. The inner tangential flow condition fails in this case at the trailing edge. Therefore, it is replaced by the condition that the normal velocity, relative to the bisector of the trailing edge angle, be zero. This condition can only be satisfied if the vorticities on the upper and lower surfaces approach the same value but with opposite signs as the trailing edge is approached. This means that the velocities have to be the same on both sides of the trailing edge. Thus the normal flow condition along with equal velocities on both sides of the trailing edge can be considered as a Kutta condition.

Unfortunately, a second singularity is caused by a finite change in the circulation around the airfoil which results in an infinite change in the velocity at the sharp trailing edge. No wonder the equation system is singular for every Kutta condition. Thus, an additional equation is required while one equation already in the equation system can be omitted. This additional equation consists of an extrapolation of the vorticity to the trailing edge and an averaging at the trailing edge. The omission of one of the equations in the system can sometimes cause errors at the point whose flow condition is governed by the omitted equation. In other words, the equation system is not exactly singular, due to small numerical approximations. So, none of the equations is omitted and the entire equation system is multiplied by the transposed matrix. This implies that all the equations are solved as accurately as possible in a least-squares sense. The results of this procedure are very precise.

The second case is a blunt trailing edge (fig. 3) - one in which the upper and lower surface trailing edge points are not the same. For this case, two different procedures have been examined.

The first procedure extends the airfoil along straight "wake limits" having constant opposite vorticity (fig. 3, top). At both the upper and lower surface trailing edge points, a normal velocity condition must be satisfied. No flow condition is satisfied in the wake.

The second procedure introduces at the base of the airfoil not only a vorticity but also a source distribution (fig. 3, bottom). Both are linear distributions over the base length and determined such that no flow singularitites occur at either of the two trailing edge points.

Both blunt trailing edge models have one more flow condition than unknown vorticities. The $n + 1$ equations for n unknowns are treated in the same manner as the sharp trailing edge case even though they are much less critical with respect to circulation changes.

For all cases the computing times are moderate; the results, very precise. A comparison of the design and the panel methods for the example airfoil is shown in figure 4.

Viscous Method

The laminar and turbulent boundary layer development is computed by a simple method (ref. 3) using, like many others, integral momentum and energy equations. It has been shown that laminar boundary layer development is predicted quite well by this method. The turbulent boundary layer routines are based upon the best availabie empirical skin friction, dissipation, and shape factor laws. No further errors are introduced by mathematical simplifications like integrating the ordinary differential equations from the momentum and energy laws by averaging the right sides of the equations.

Of special interest are the predictions of transition from laminar to turbulent boundary layer and the separation of the turbulent boundary layer. The tendency toward separation is determined solely by the shape factor

$$H_{32} = \frac{\delta_3}{\delta_2}$$

where δ_3 is energy thickness and δ_2 is momentum thickness. (Note that H_{32} has the opposite tendency from H_{12} which contains the displacement thickness δ_1 instead of the energy thickness.) For laminar boundary layers there exists a constant and reliable lower limit of H_{32}, which equals 1.515 and corresponds to laminar separation. For turbulent boundary layers no such unique and reliable limit has been determined. It can be stated, however, that the turbulent boundary layer will separate if H_{32} goes below 1.46 and will not separate if H_{32} remains above 1.58. It has been noticed that thicker boundary layers tend to separate at lower H_{32} values. In the present method, turbulent separation is predicted if H_{32} drops to 1.46. This is a fairly good assumption because the method usually predicts relatively low values of H_{32}. The uncertainty is not as bad as it first appears in that H_{32} changes rapidly near separation. Nevertheless, results must be checked carefully with respect to turbulent separation.

The second feature of special interest is the prediction of transition. Two different procedures are in vogue today - the amplification method and the shape-factor — Reynolds-number method. The first procedure requires much more computing time because many frequencies must be traced to find the one wave which is suddenly amplified to the ratio set as the transition limit. The better procedure cannot be selected until we know more about transition. The differences between the two procedures are small for normal airfoil applications as the local Reynolds number changes quickly near transition. So, we still use the simple criterion shown in figure 5. Thus, the transition Reynolds number depends only on the shape factor H_{32}. Adverse pressure gradients and, hence, low values of H_{32} result in lower transition Reynolds numbers and vice versa. As will be seen later, it is very informative to plot the boundary layer development in this form.

It must be pointed out that the boundary layer development immediately after transition has a significant influence on the entire flow. In our program the prediction of transition results in a switch from the laminar skin friction, dissipation, and shape factor laws to the turbulent ones, without changing H_{32} and δ_2. This is also done if laminar separation is predicted before the transition criterion is reached. The H_{32} development

for the linearly decreasing velocity distribution defined by

$$V = V_\infty(1 - x/l)$$

is shown in figure 6 for Reynolds numbers ranging from 0.125×10^6 to 32×10^6 where Reynolds number $R = V_\infty l/\nu$. This plot illustrates the well-known fact that the laminar boundary layer shape factor H_{32} and laminar separation are independent of Reynolds number. It also shows that for high Reynolds numbers, transition occurs before laminar separation. For turbulent boundary layers, H_{32} and separation do depend on Reynolds number. The most important information to be gained from figure 6 is the behavior of H_{32} at the beginning of the turbulent boundary layer. For higher Reynolds numbers, H_{32} increases immediately to values greater than about 1.7. For lower Reynolds numbers this increase is less rapid and the maximum values of H_{32} are lower. For a Reynolds number of 0.125×10^6, H_{32} remains below 1.58 which means that the method cannot determine whether or not an attached turbulent boundary layer exists. Such results must be studied in more detail. In figure 7 the laminar and turbulent skin-friction laws, $C_f(R_{\delta_2}, H_{32})$ are presented. The laminar law has an exponent of -1. The turbulent law is a slightly modified Ludwieg-Tillman law with an exponent of -0.232. This law is experimentally derived and tested for R_{δ_2} between 10^3 and 10^5 as shown by the phantom lines in figure 7. Below R_{δ_2} equal to 10^3, these lines continue in some manner. The flat plate case has been investigated in more detail and the results indicate that the flat plate line continues more or less steadily and finally bends down to the laminar law line rather steeply, depending on roughness and free-stream turbulence.

In our method, the Ludwieg-Tillman law is extrapolated along straight lines. This probably represents an upper limit for C_f for R_{δ_2} less than 10^3. But it is obvious that for R_{δ_2} equal to 10^2 the laminar and turbulent laws differ little and for lower R_{δ_2} the turbulent C_f values are below the laminar ones.

For results such as those shown in figure 6, it is interesting to look at the C_f values computed by our method. For every point x/l, R_{δ_2} and H_{32} are known and, hence, C_f is known. The variation of C_f with R_{δ_2} is shown in figure 7. The result is remarkable. The curves for $R = 0.125 \times 10^6$ and $R = 0.25 \times 10^6$ do not even come close to an area where one can confidently speak of a turbulent skin-friction law. Such "underdeveloped" turbulent boundary layers exist in nature only in the form of laminar separation bubbles. After examining many different cases, it was determined that there is a certain

analogy between the predicted "underdeveloped" turbulent boundary layers with low H_{32} values and laminar separation bubbles. The boundary layer results computed by our method show a stronger bubble analogy as Reynolds number decreases and as the adverse pressure gradient after transition becomes steeper. If the analogy occurs in the results, the only way to alleviate it is to reduce the adverse pressure gradient after transition. The experimental results for laminar separation bubbles show the same tendencies. Accordingly, it is very helpful to have this bubble analog in the computed results.

In summary, the boundary layer method has generated good results for many, very different cases. It should be noted, however, that no fundamental problem exists in replacing the boundary layer subroutines in our program with other subroutines. Some applications will be discussed in the next section. But before that a few comparisons with other boundary layer methods will be made.

Two shape factor developments computed by a program written by Konhauser, which uses the Cebeci-Smith method (ref. 4), are shown by dashed curves in figure 6. The two curves, which are for the Reynolds numbers of 8×10^6 and 16×10^6, agree quite well with the present method for x/l up to about 0.2. Then as x/l increases, the results computed by the Cebeci-Smith method show considerably less tendency toward separation. This demonstrates that the separation limit of H_{32} equal to 1.46 that we use is conservative with respect to turbulent separation. Comparisons for lower Reynolds numbers are not possible at this time because Mr. Konhauser has been unable to obtain results from the Cebeci-Smith method at lower Reynolds numbers.

The development of displacement thickness along the upper surface of an RAE 101 airfoil for an angle of attack of 8.2^0 and a Reynolds number of 1.6×10^6 is shown in figure 8. This case was computed by J. L. Hess using a Cebeci-Smith program with different numbers of elements and different smoothing procedures (ref. 5). The results from the program as indicated by the symbols agree very well with those computed by Hess with the greatest number of elements. This agreement is remarkable indeed knowing that this is the first comparison of this type which we have made and is not the result of a careful choice of data.

The curves in figure 9 demonstrate that, in using integral momentum and energy laws, the introduction of mathematical simplifications can cause much larger errors than those which result from the use of a one parameter method. In figure 9, our method and a method developed by L. Truckenbrodt (ref. 6) are compared with experimental results obtained by Wortmann (ref. 7). Truckenbrodt's method is based upon the same skin-friction and dissipation laws as the present method, but includes further mathematical simplifications which produce an error of about 50 percent for the adverse pressure gradient shown.

In the present method, the momentum thickness at the trailing edge is used for the calculation of the drag by a Squire-Young type formula. We have found that our method predicts slightly higher drag values than those measured

experimentally. We hesitate to change the skin-friction laws or other parts of the program, however, as the differences between our predictions and experimental measurements depend upon the wind tunnel in which the experiments were performed. (See figs. 10 and 11.)

It should be mentioned that the program includes a lift coefficient correction due to boundary layer separation but, as yet, does not include one due to boundary layer displacement thickness.

As a final remark, the development of the laminar boundary layer should be discussed. It is very informative to plot this development as shown in figure 5. This plot reveals several important points. For a constant velocity segment ($\alpha = \alpha^*$), the boundary layer approaches the Blasius solution having a shape factor H_{32} of 1.573 and increasing momentum thickness δ_2. This corresponds to the vertical lines in figure 5. As the angle of attack is increased, the velocity distributions become concave over the forward portion of the airfoil or, in other words, the airfoil "pulls a peak" at the leading edge. These concave distributions are similar to those which produce Hartree boundary layers. But, whereas the Hartree boundary layers result in lower but still constant shape factors, the curves in figure 5 show increasing H_{32} with increasing R_{δ_2} for α greater than α^*. This means that these velocity distributions are more concave than the Hartree (power law) distributions. Thus, as the angle of attack is increased even more, these distributions will result in laminar separation at the leading edge. This problem is eliminated by the introduction of segments having higher α^* values near the leading edge. Obviously, it is much easier to control the development of the shape factor by manipulating α^* values than by changing a given velocity distribution at only one angle of attack.

Applications

In this section, we shall apply the mathematical model to a variety of airfoil problems. The final result is always a plot which includes c_l versus c_d, c_l versus α, c_m versus α, and transition and separation versus c_l as is normally plotted for wind tunnel results. It is, of course, very easy to obtain more details such as pressure distributions, boundary layer development, and laminar separation bubble analogs.

The first application is a sailplane airfoil designed for low drag at a Reynolds number of about 3×10^6 and a soft stall at a Reynolds number of about 1×10^6. The soft stall can easily be achieved by introducing a moderate concave pressure recovery on the upper surface and by preventing laminar separation and the rapid forward movement of transition with increasing angle of attack. The latter feature requires only increasing α^* values toward the leading edge.

The theoretical results agree well with the experimental measurements obtained by D. Althaus as shown in figure 10. In the wind tunnel experiment, transition location was determined by the stethoscope method which seems to detect only fully developed turbulence and, thus, the experimental transition locations lie somewhat downstream of the theoretical ones although the trends with angle of attack agree well. The stall observed in free flight was very soft.

The next application shows that the program produces reasonable results for higher Reynolds numbers as well. The coordinates of an NACA 64_3-618 airfoil were input and the theoretical results are compared with the experimental measurements (ref. 8) in figure 11.

The program can also be applied at very low Reynolds numbers. Airfoil 387 was designed for model airplanes. At these low Reynolds numbers, the bubble analog indicated that only very slight adverse pressure gradients were possible and, accordingly, a relatively thin airfoil (t/c = 0.09) resulted. This airfoil was recently tested by Volkers (ref. 9). The theoretical results compare favorably with experiment for a Reynolds number of 2×10^5 (fig. 12), even though the measurements do show the typical effect of laminar separation bubbles. For a Reynolds number of 1×10^5, the experiment shows even more the effect of laminar separation bubbles, but still with attached turbulent flow at the trailing edge. For a Reynolds number of 6×10^4, both experiment and theory indicate a large amount of separation. It seems remarkable that the experimentally determined critical Reynolds number agrees so well with that predicted by the theory.

High lift airfoils can also be designed and analyzed with the program. One such airfoil designed by Chen (ref. 10) is shown in figure 13. Notice that the panel method has predicted some oscillations in the velocity distributions. (The occurrence of these oscillations is common for the newer airfoil designs as opposed to the older NACA airfoils for which the panel method predicts smooth velocity distributions.) The objective of this airfoil design was to achieve on the upper surface a certain length of constant velocity followed by a Stratford pressure recovery (ref. 11). The boundary layer development for this airfoil showed early transition due to the oscillations in the velocity distributions. These results, of course, were unrealistic and, accordingly, a new airfoil, 1220, was designed with the same objective (fig. 14). To demonstrate that the oscillations in the velocity distributions for the Chen airfoil were not produced by the panel method, the velocity distributions from the panel method are included for the new airfoil.

The boundary layer results for this airfoil are quite interesting. If the transition point is just ahead of the pressure recovery, the predicted boundary layer remains attached until the closure contribution is reached. This occurs at a Reynolds number of 6×10^6 (fig. 15). This demonstrates that the method predicts the boundary layer development for an extreme pressure recovery quite well. (This had already been tested by M. Schulz.) At a Reynolds number of 3×10^6, an intense laminar separation bubble was predicted at the beginning of the pressure recovery. At a Reynolds number of 9×10^6,

transition is predicted further ahead of the pressure recovery and a thicker (turbulent) boundary layer arrives at the beginning of the pressure recovery than if the flow had remained laminar up to that point. And so, again the precise initial conditions for the Stratford pressure recovery are not satisfied and early turbulent boundary layer separation is again the result. This must be true for every airfoil having a Stratford pressure recovery derived from one initial condition.

Accordingly, a new airfoil was designed which would not exhibit the undesirable characteristics of the previous airfoil. Because maximum lift normally occurs, in flight, at lower Reynolds numbers, the objective of the new design was to develop a high lift coefficient at a Reynolds number of 1×10^6 while still maintaining a soft stall for practical reasons. The airfoil which resulted is shown in figure 16. The α^* distribution for the forward portion of the upper surface was chosen such that no sudden movement of laminar separation or transition is possible. This feature is demonstrated in figure 17 in which all the curves show decreasing H_{32} with increasing R_{δ_2}. The pressure recovery is concave but not nearly as extreme as the Stratford distribution. It should be mentioned that the total amount of pressure recovery for this distribution is only slightly less than that of the Stratford distribution. Thus, the moderate pressure recovery results in more lift.

Another feature of this design is that the upper and lower surface velocities ahead of the closure contribution were not required to be equal as in the case of the Chen airfoil. It has already been demonstrated by the NACA 6-series airfoils that this condition is not necessary.

The theoretical results for this new airfoil are shown in figure 18. The maximum lift coefficients to be achieved by such airfoils are surely above 2.

CONCLUSIONS

The present program system of combined potential flow and boundary layer theories has been discussed. Applications and comparisons with experiments over a very wide range of Reynolds numbers have been shown. The results are most satisfactory and open the door to the tailoring of airfoils for specific objectives.

REFERENCES

1. Eppler, R.: Direct Calculation of Airfoils From Pressure Distribution. NASA TT F-15417, 1974.

2. Eppler, R.: Results of the Combined Application of Boundary Layer and Profile Theory. NASA TT F-15416, 1974.

3. Eppler, R.: Praktische Berechnung Laminarer und Turbulenter Absauge-Grenzschichten (Practical Calculation of Laminar and Turbulent Suction Boundary Layers). Ingenieur-Archiv, Bd. 32, 1963, pp. 221-245.

4. Cebeci, T.; and Smith, A. M. O.: Analysis of Turbulent Boundary Layers. Academic Press, 1974.

5. Hess, J. L.: A Fully Automatic Combined Potential-Flow Boundary-Layer Procedure for Calculating Viscous Effects on the Lifts and Pressure Distributions of Arbitrary Three-Dimensional Configurations. MDC J7491, Douglas Aircraft, 1977.

6. Truckenbrodt, E.: Ein Quadratur-Verfahren zur Berechnung der Laminaren und Turbulenten Reibungsschicht fuer Zweidimensionale und Axialsymmetrische Stroemung. Ingenieur-Archiv, Bd. 20, 1952, pp. 211-228.

7. Wortmann, F. X.: A Contribution to the Design of Laminar Profiles for Gliders and Helicopters. TIL/T.4903, British Ministr. Aviat., Feb. 1960.

8. Abbott, I. H.; Von Doenhoff, A. E.; and Stivers, L. S., Jr.: Summary of Airfoil Data. NACA Rep. 824, 1945.

9. Volkers, D. F.: Preliminary Results of Windtunnel Measurements on Some Airfoil Sections at Reynolds Numbers Between 0.6 x 10^5 and 5.0 x 10^5. Memorandum M-276, Delft University of Technology, Department of Aerospace Engineering, The Netherlands, 1977.

10. Bingham, G. J.; and Chen, A. W.: Low-Speed Aerodynamic Characteristics of an Airfoil Optimized for Maximum Lift Coefficient. NASA TN D-7071, 1972.

11. Stratford, B. S.: The Prediction of Separation of the Turbulent Boundary Layer. J. Fluid Mech., vol. 5, pt. 1, Jan. 1959, pp. 1-16.

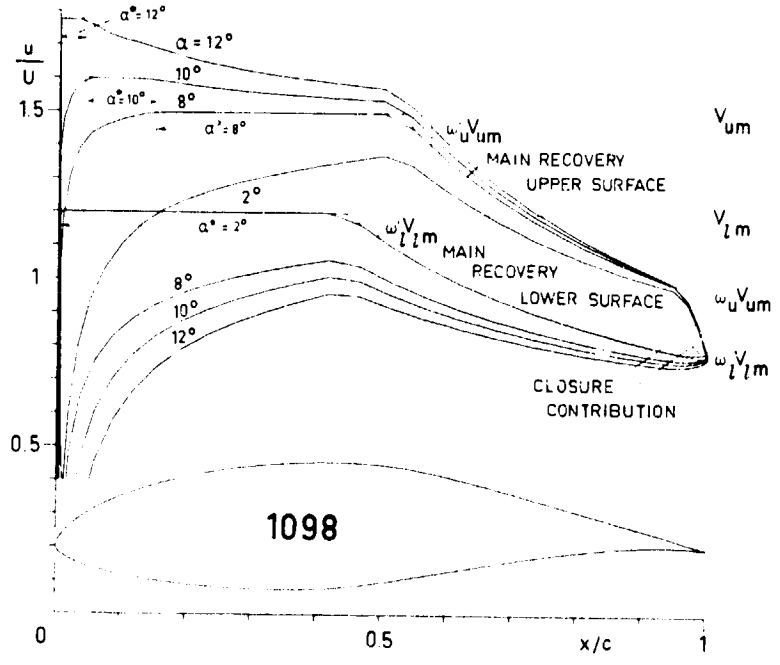

Figure 1.- Design method. (α relative to zero-lift line.)

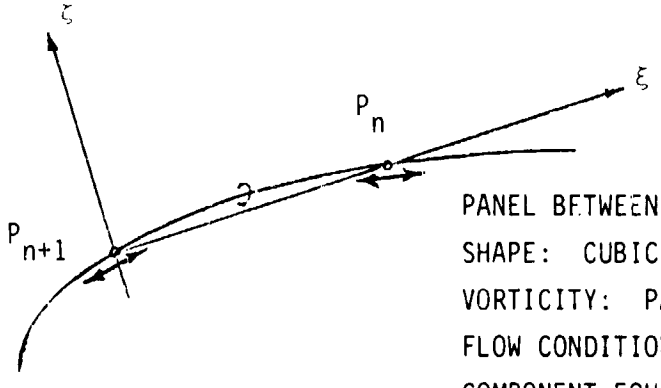

PANEL BETWEEN P_n AND P_{n+1}:
SHAPE: CUBIC
VORTICITY: PARABOLIC
FLOW CONDITION: INNER TANGENTIAL FLOW
COMPONENT EQUALS ZERO AT P_n AND P_{n+1}

Figure 2.- Panel method.

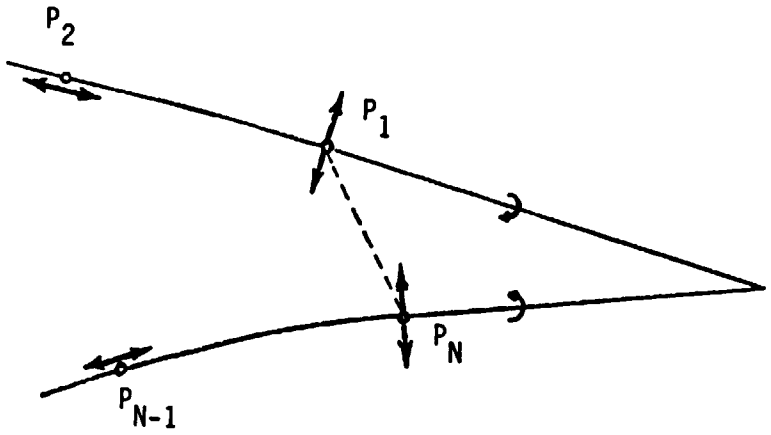

WAKE 1: $P_N = -P_1$ (KUTTA-CONDITION)
TRIANGULAR WAKE WITH CONSTANT OPPOSITE VORTICITY
NORMAL FLOW CONDITION AT P_1 AND P_N
NO FLOW CONDITION AT THE WAKE

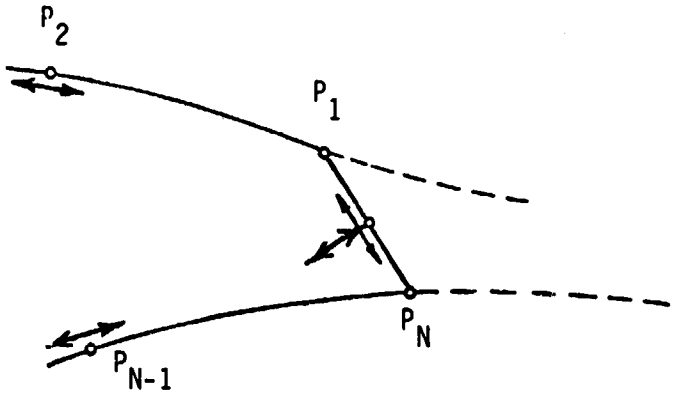

WAKE 2: $P_N = -P_1$ (KUTTA)
LINEAR VORTICITY AND SOURCE DISTRIBUTION AT THE BASE SUCH THAT NO FLOW SINGULARITY EXISTS AT P_1 AND P_N. FLOW CONDITIONS: INNER TANGENTIAL AND INNER NORMAL VELOCITY EQUALS ZERO AT THE MIDDLE OF THE BASE

Figure 3.- Blunt trailing edge.

C-2

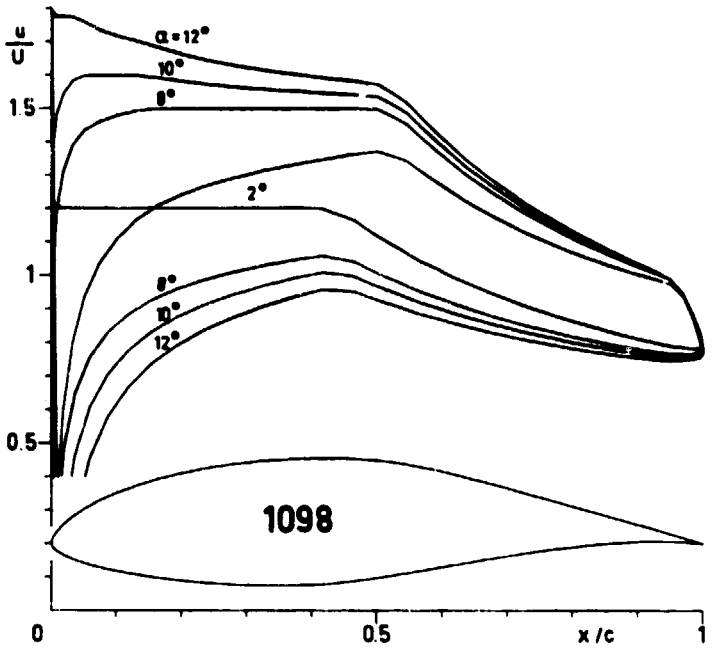

Figure 4.- Comparison of design and panel methods. (α relative to zero-lift line.)

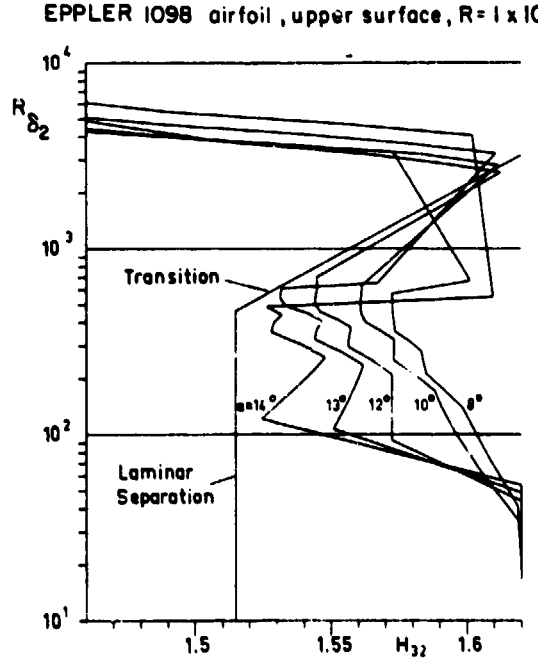

Figure 5.- Boundary layer development.

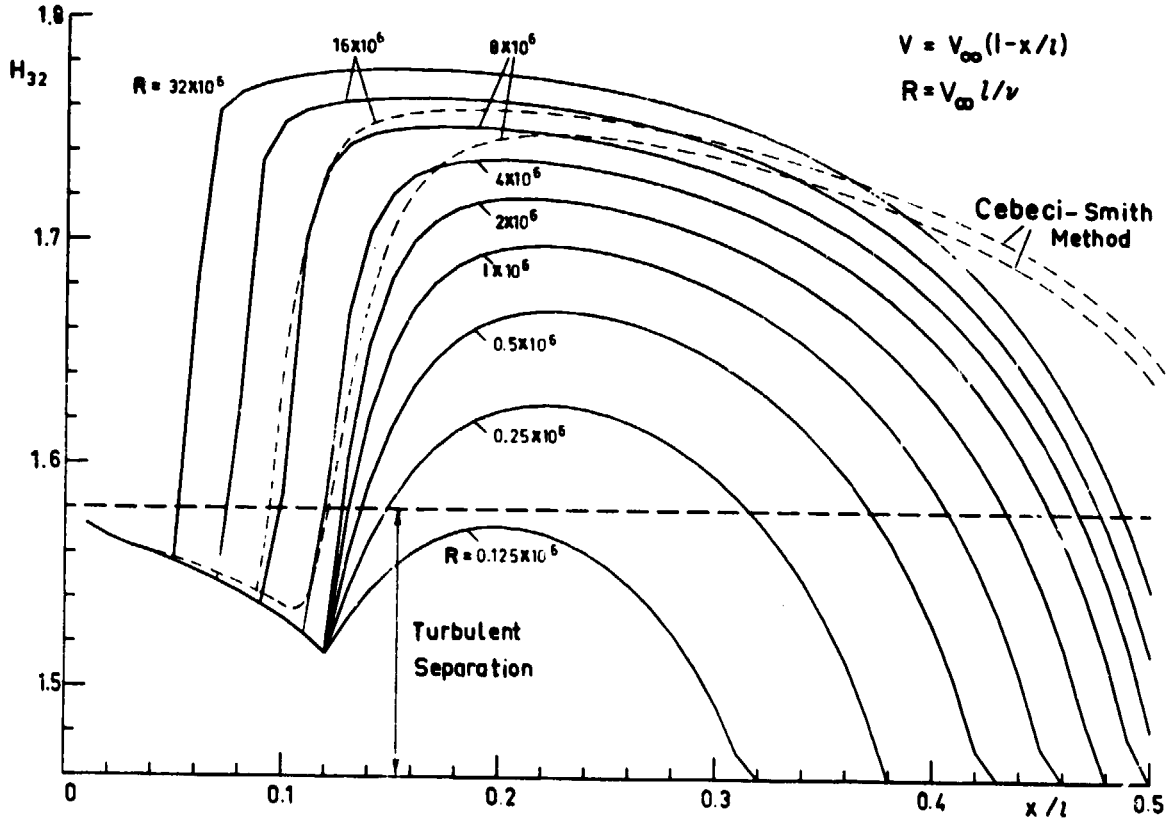

Figure 6.- Comparison of short-cut and finite-difference methods.

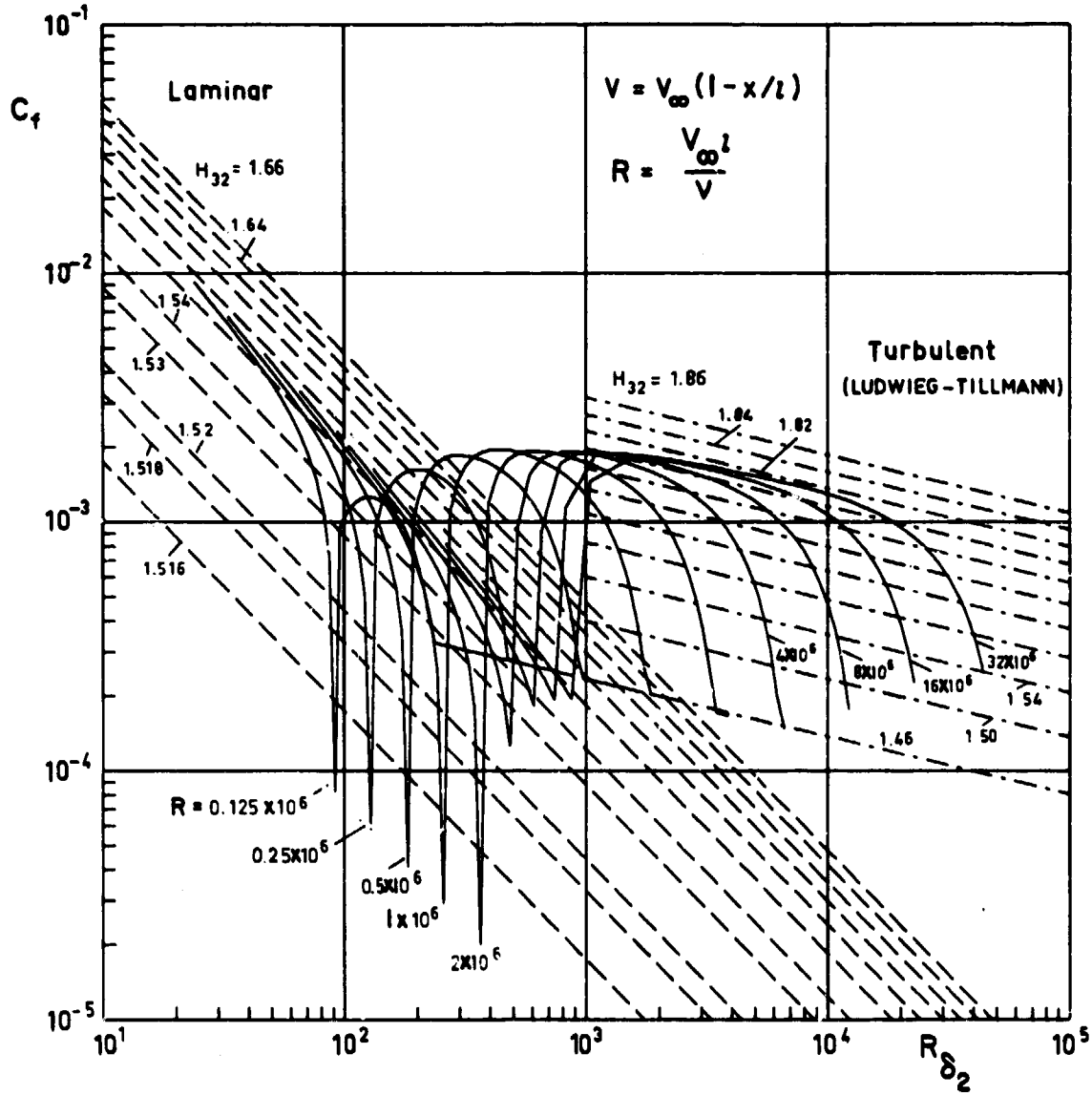

Figure 7.- Skin-friction coefficients.

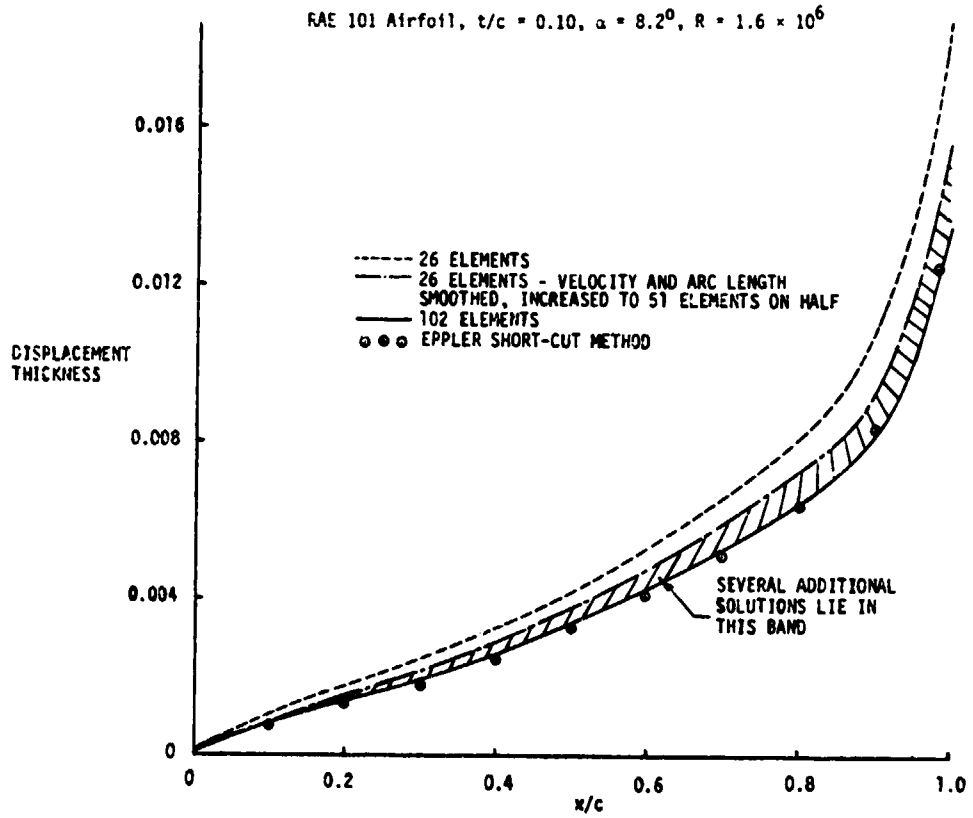

Figure 8.- Comparison of displacement thicknesses.

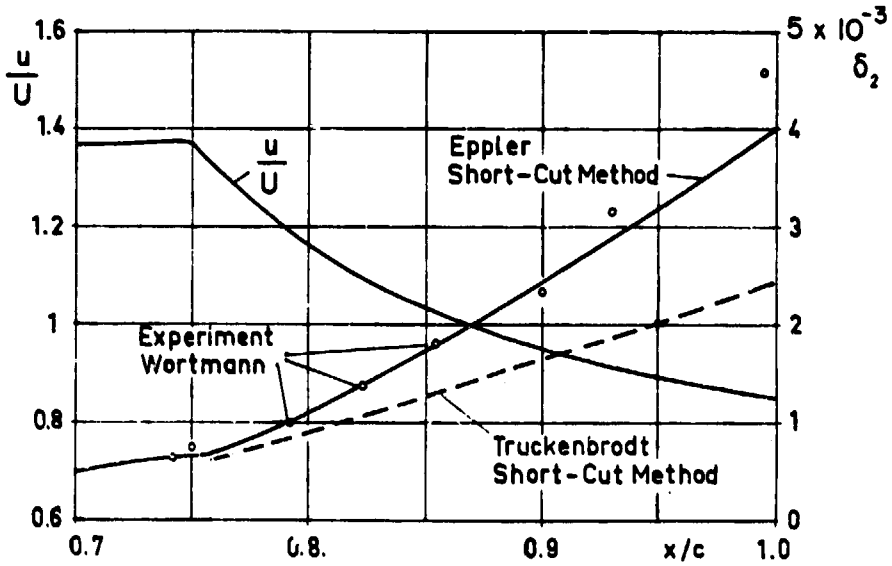

Figure 9.- Comparison of momentum thicknesses.

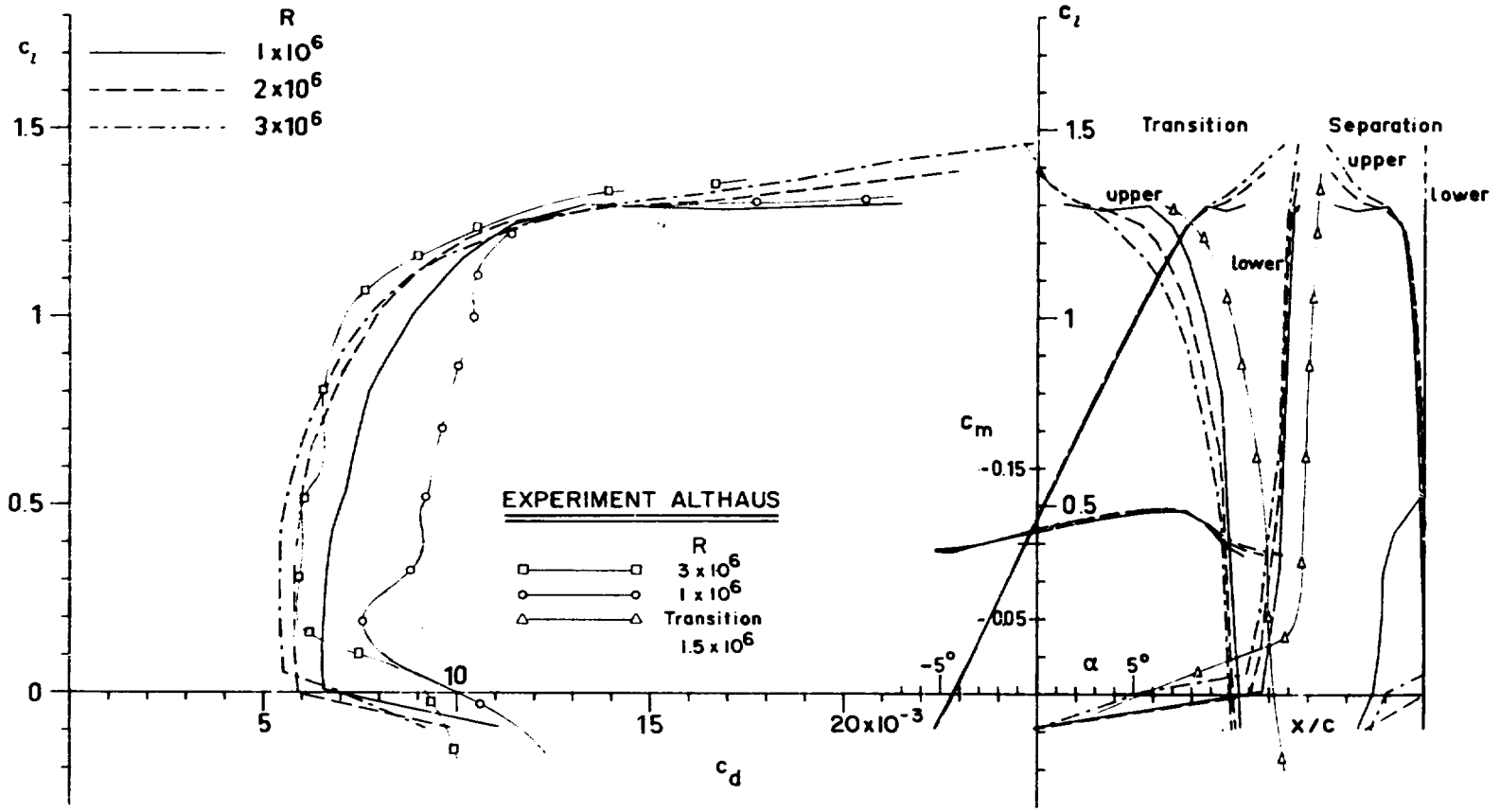

Figure 10.- Comparison of experiment and theory for EPPLER 603 airfoil.

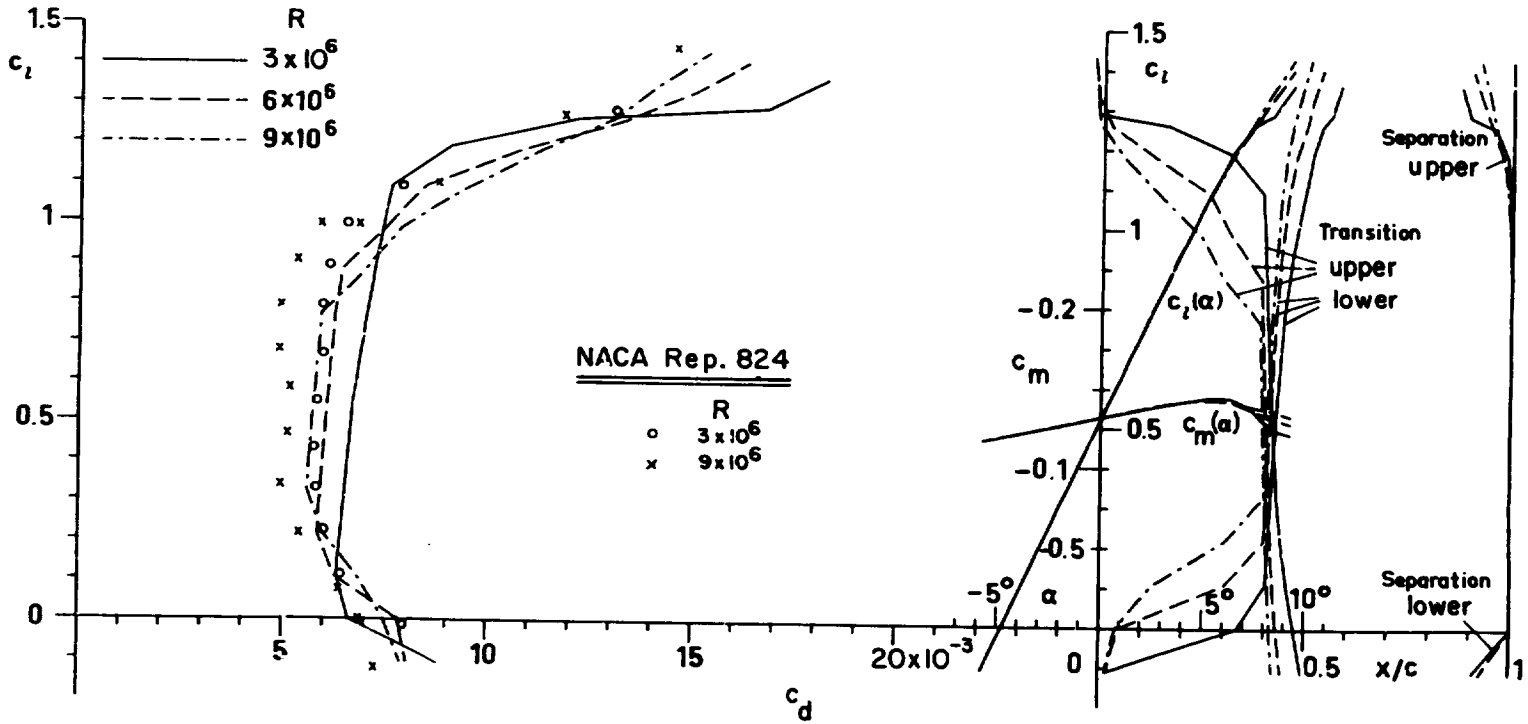
R
3x10^6
6x10^6
9x10^6
NACA Rep. 824
R
3x10^6
9x10^6
Separation upper
Transition upper lower
Separation lower
Figure 11.- Comparison of experiment and theory for NACA 64$_3$-618 airfoil.

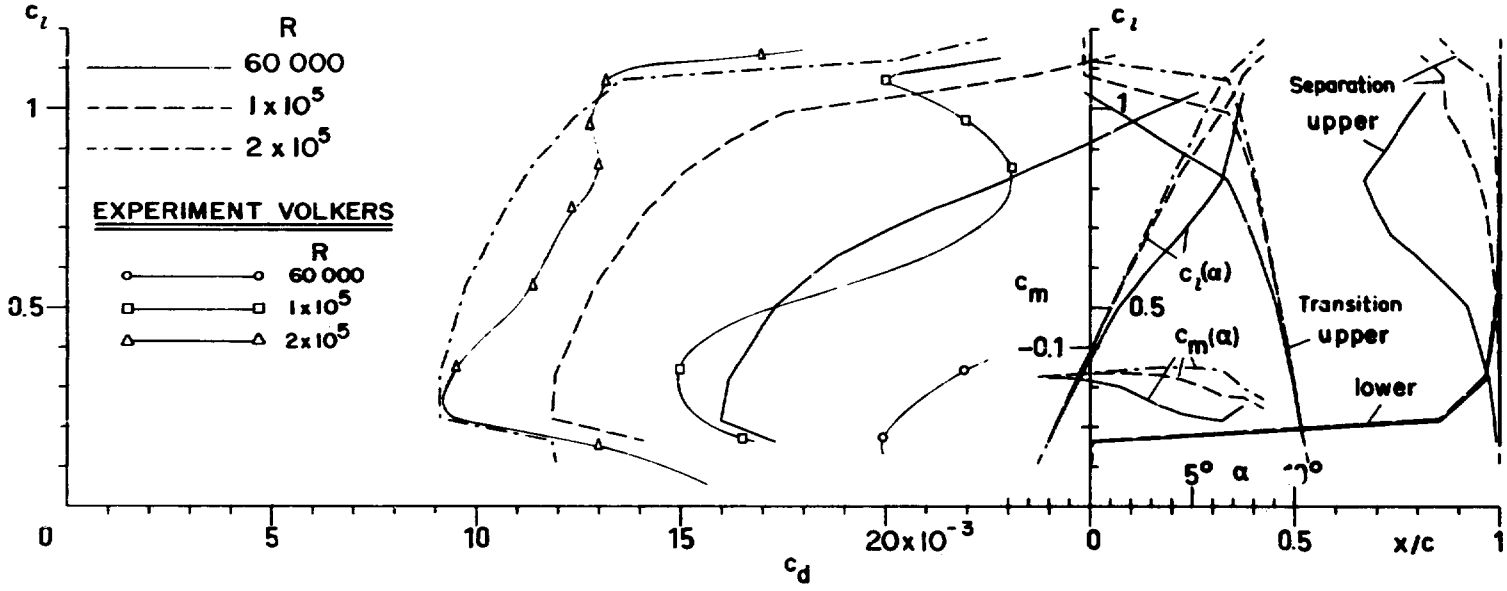

Figure 12.- Comparison of experiment and theory for EPPLER 387 airfoil.

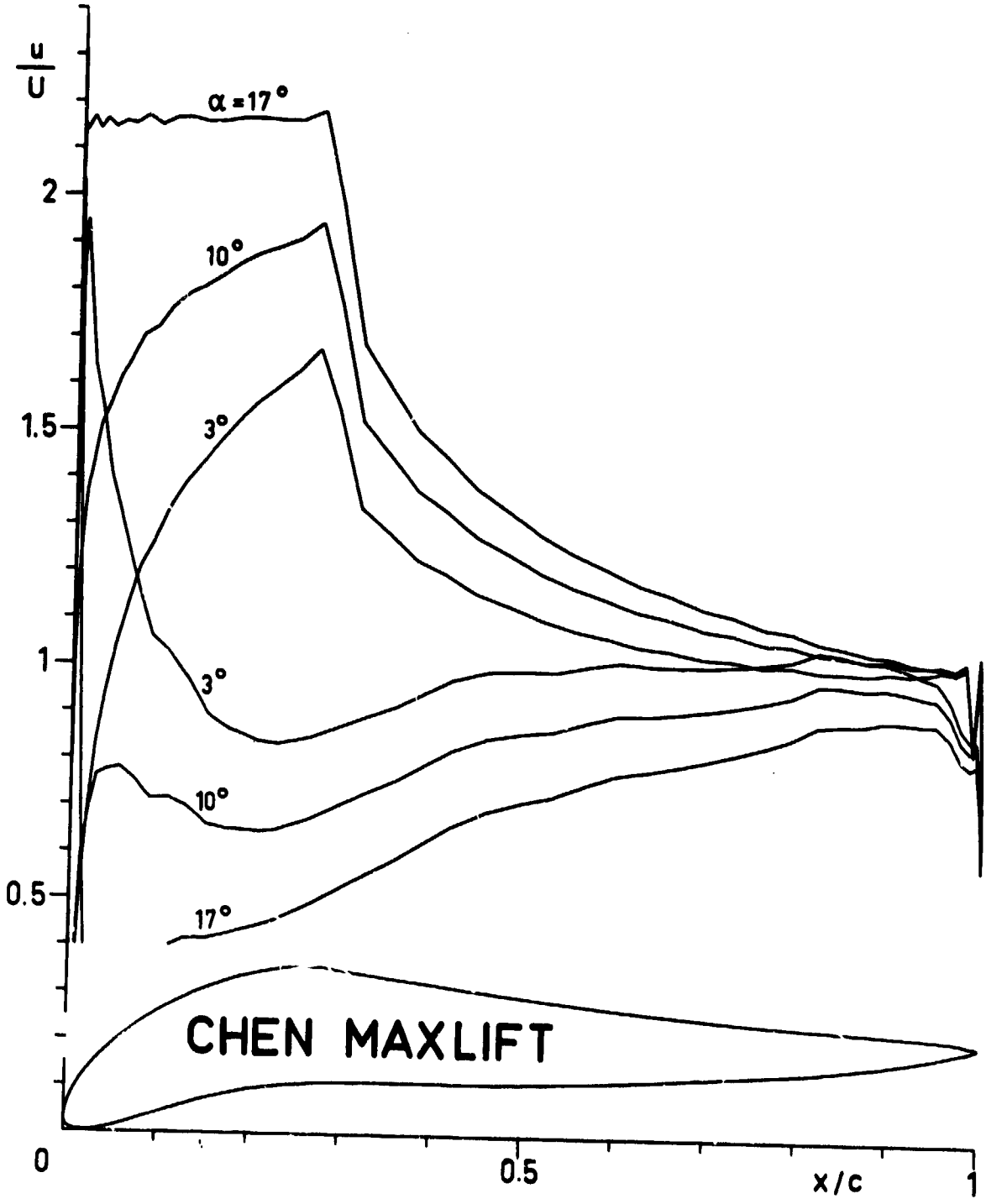

Figure 13.- Chen maximum lift airfoil. (α relative to zero-lift line.)

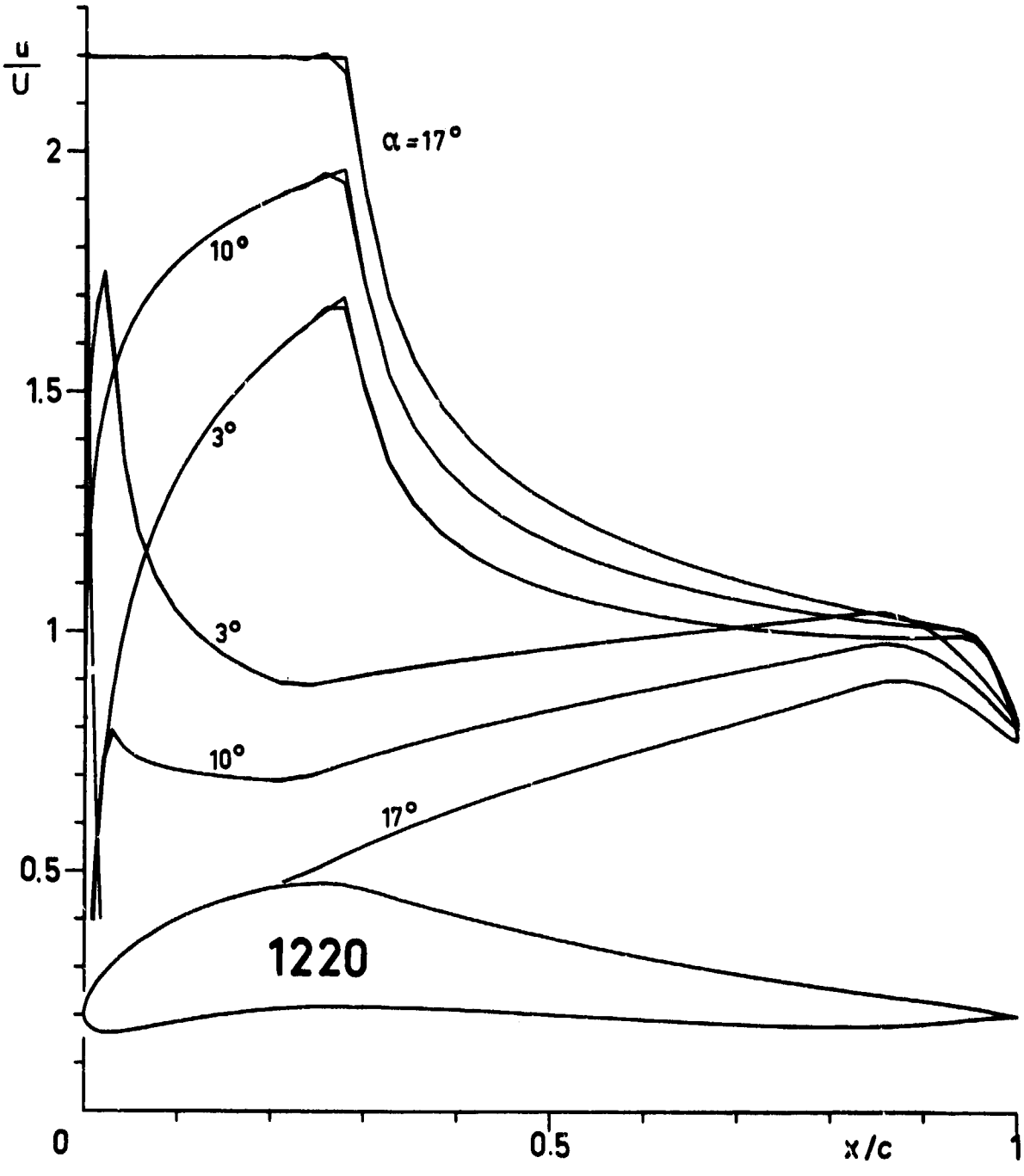

Figure 14.- EPPLER 1220 airfoil. (α relative to zero-lift line.)

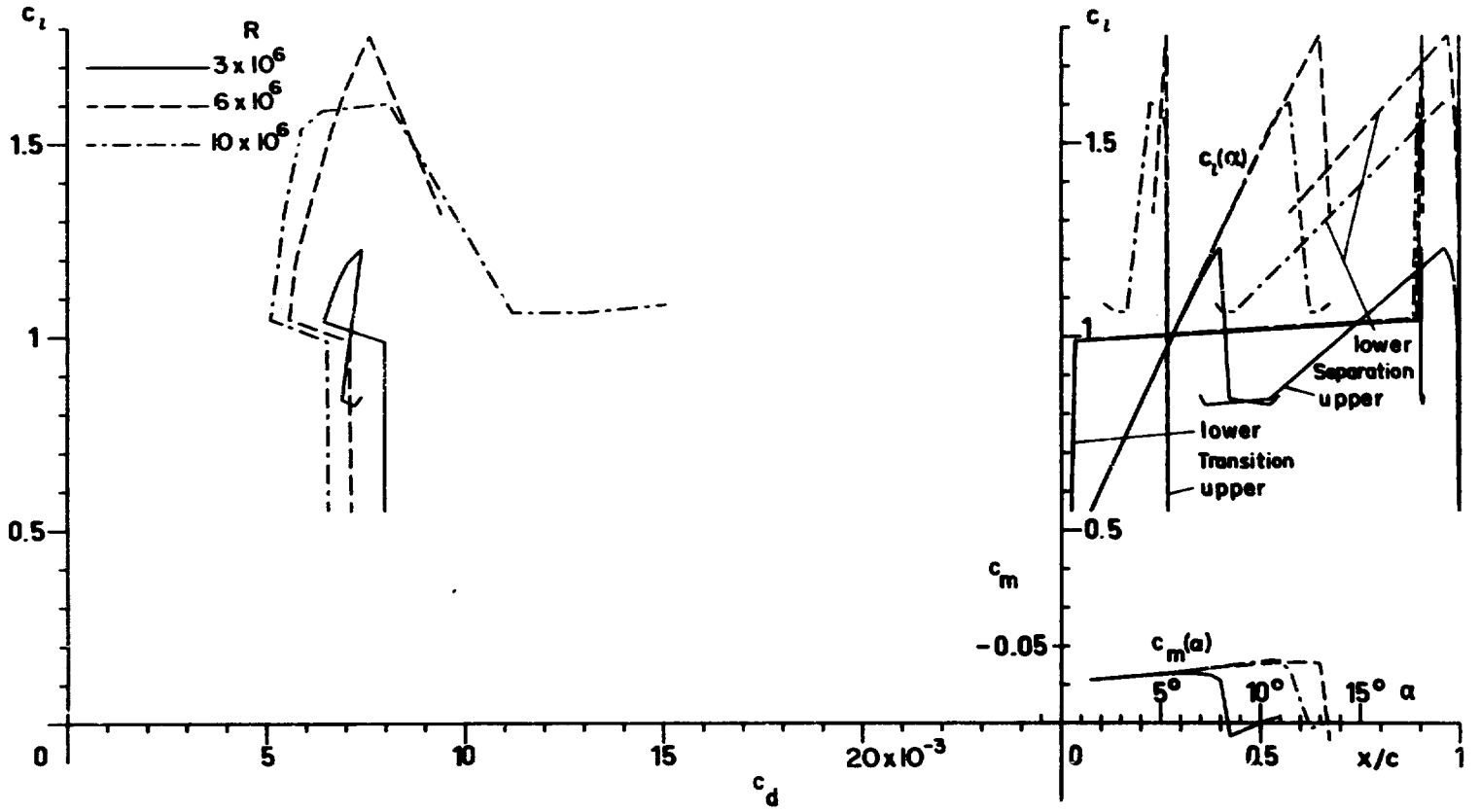

Figure 15.- Theoretical results for EPPLER 1220 airfoil.

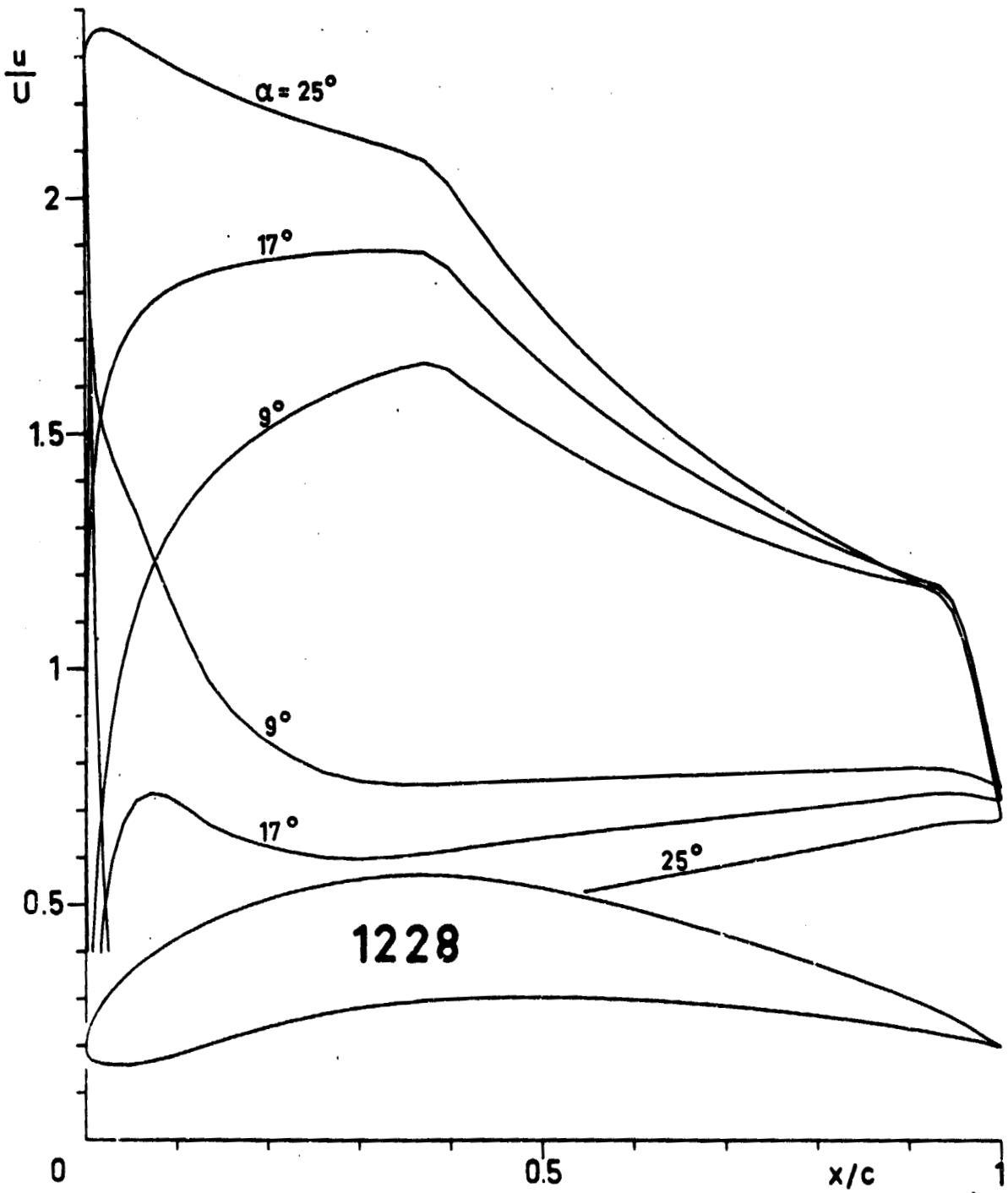

Figure 16.- EPPLER 1228 airfoil. (α relative to zero-lift line.)

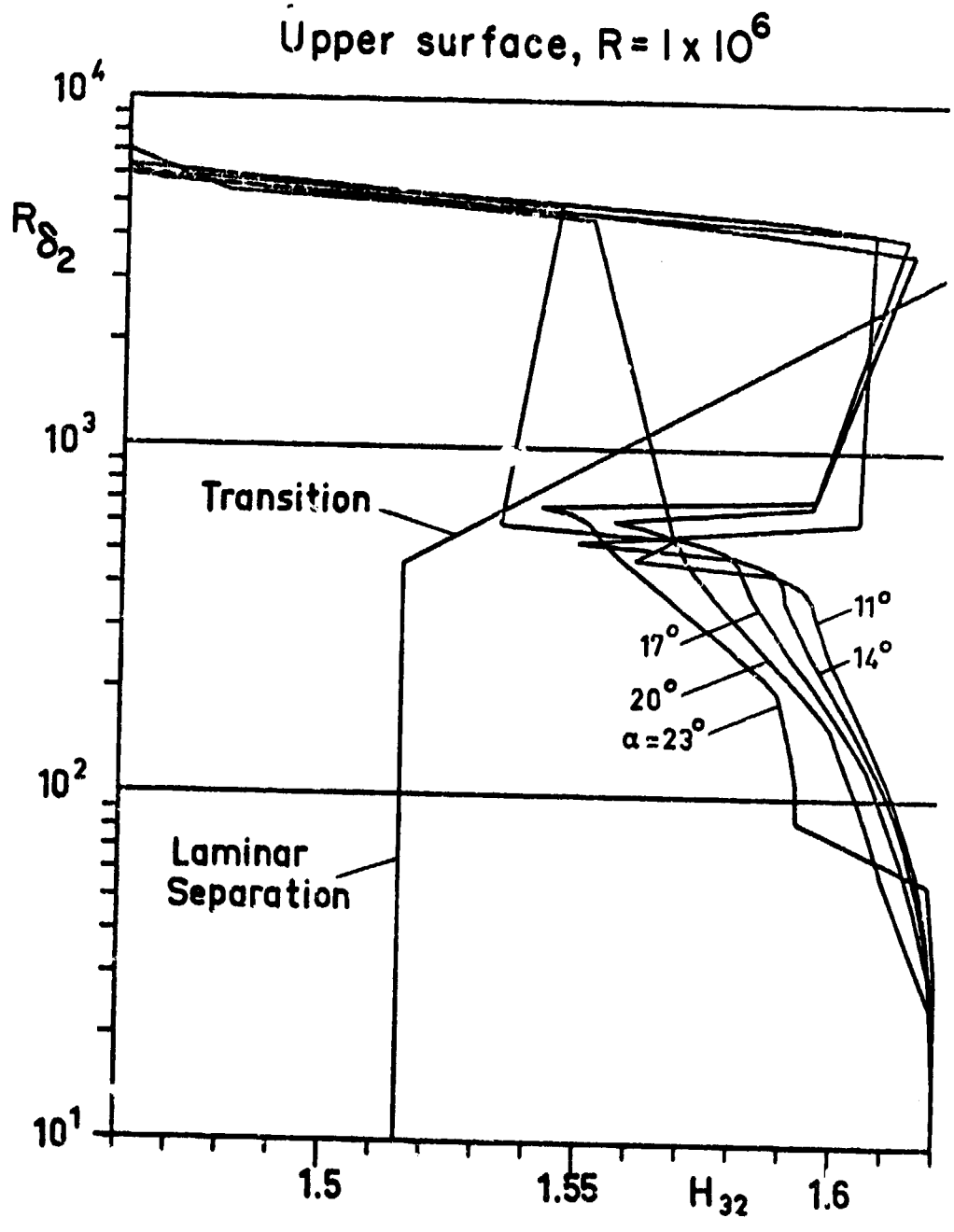

Figure 17.- Boundary layer development for EPPLER 1228 airfoil.

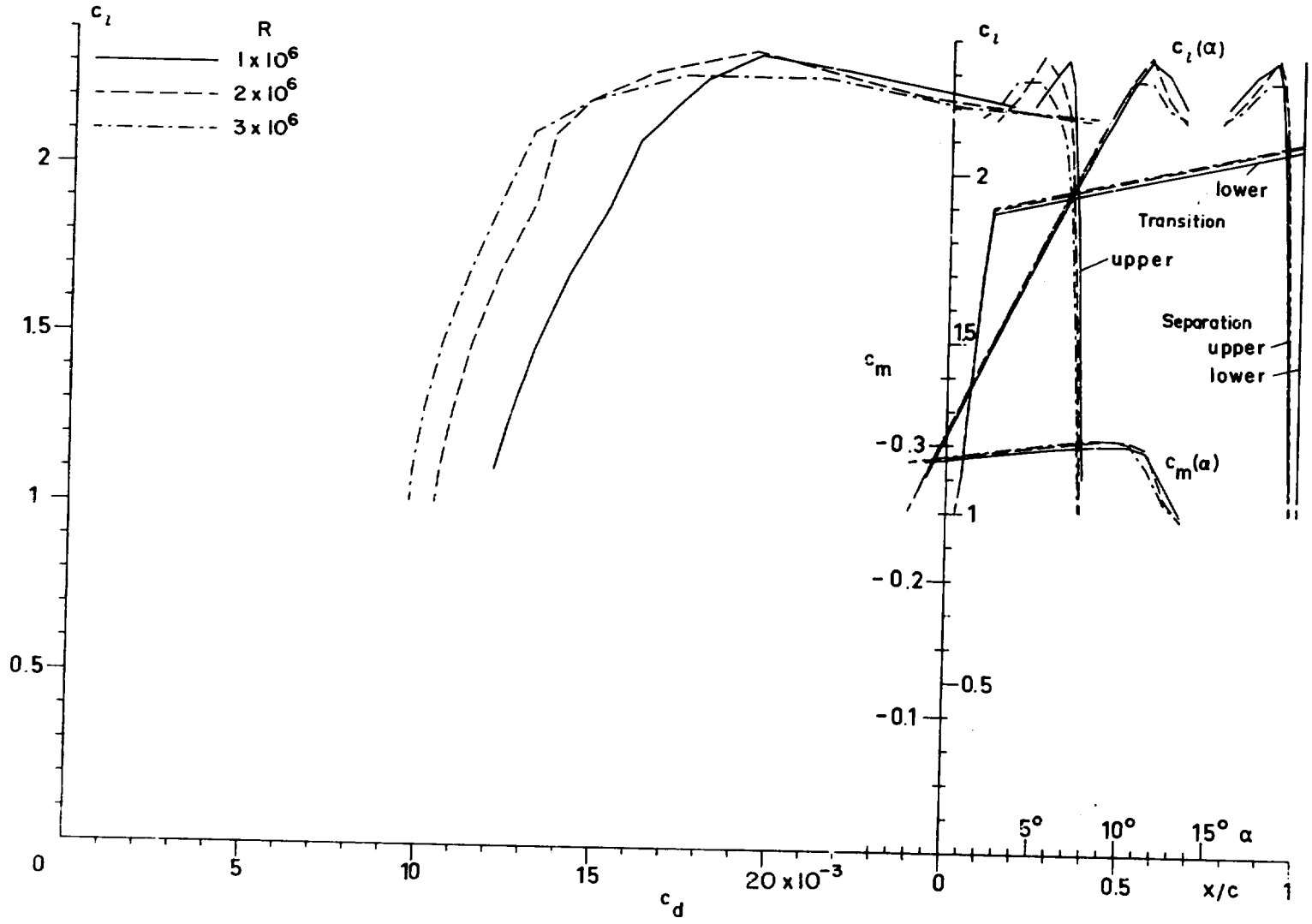

Figure 18.- Theoretical results for EPPLER 1228 airfoil.